RESEARCH   **Open Access**

Macrocell Corrosion Currents in Simulated Concrete Pore Solution and Reinforced Concrete

Josep Ramon Lliso-Ferrando[1*] , Isabel Gasch[1], Ana Martínez-Ibernón[1] and Manuel Valcuende[2]

Abstract

Chloride-induced rebar corrosion is one of the main causes of damage in reinforced concrete structures (RCS). Chloride attacks lead to depassivation creating pits, which can imply major losses of sections. The current generated at these spots (microcell) is contributed by the current produced between corroded and uncorroded areas (macrocell). The influence of both currents has been deeply investigated based on solution studies, which do not actually represent the behaviour of concrete-embedded elements. The studies about macrocell currents in solution are interesting to analyse this phenomenon quickly and simply. However, they must not be interpreted as the reality of RCS because this requires studies using rebars embedded in concrete. The performed experimental plan verified this fact. In addition, another objective of this study was to analyse the influence of concrete's electrical resistance and the limiting effect of the cathode/anode surface (Cs/As) ratio on macrocell currents in solution and in concrete. For this study, specimens manufactured using concretes with different properties were used: standard concrete (SC), high-performance concrete (HPC), very high-performance concrete (VHPC) and ultra-high performance-fibre reinforced concrete (UHPFRC). The conclusions show how the Cs/As ratio plays a key role in regulating macrocell current intensity, but what really governs this phenomenon is concrete resistivity because it regulates the participation of a bigger or smaller cathode surface. The influence of this parameter as a limiting factor of macrocell currents is fundamental, especially in high resistivity concretes like VHPC and UHPFRC.

Keywords Reinforced concrete structures, Macrocell corrosion, Concrete resistivity, Durability

1 Introduction

Chloride-induced rebar corrosion is one of the main causes of early failure in reinforced concrete structures (RCS) located in a marine environment or in places where de-icing salt is spread (Altoubat et al., 2016; Ayinde et al., 2019; Behera et al., 2016; Poursaee & Hansson, 2009; Zhou et al., 2015). The presence of chlorides

above the critical content (C_{crit}) at the depth where rebars are located leads to their depassivation (Angst et al., 2011; Morga & Marano, 2015; Sangoju et al., 2011) which, under favourable thermodynamic conditions, can trigger active rebar corrosion. This critical chloride content has been well-studied, but no general agreement about a C_{crit} value has been reached (Alonso et al., 2000; Angst et al., 2009; Cao & Cheung, 2014; Polder, 2009; Trejo & Monteiro, 2005). However, chloride anion diffusion in concrete does not take place uniformly because of the material's heterogeneity. This might mean that the chloride concentration reaching the rebar is not the same over the entire surface, which results in pitting corrosion processes (Diao et al., 2012; Li et al., 2019).

Pitting corrosion on rebars leads to major losses of the sections at these points (Andrade et al., 2008). This phenomenon accelerates as much smaller the anode

*Correspondence:
Josep Ramon Lliso-Ferrando
jollife2@arq.upv.es
[1] Research Institute for Molecular Recognition and Technological Development (IDM), Electrochemistry Laboratory, 1B-ETSIE, Universitat Politècnica de València, Camino de Vera, s/n., 46022 Valencia, Spain
[2] Department of Architectural Constructions, School of Architecture, Electrochemistry Laboratory, 1B-ETSIE, Universitat Politècnica de València, Camino de Vera, s/n., 46022 Valencia, Spain

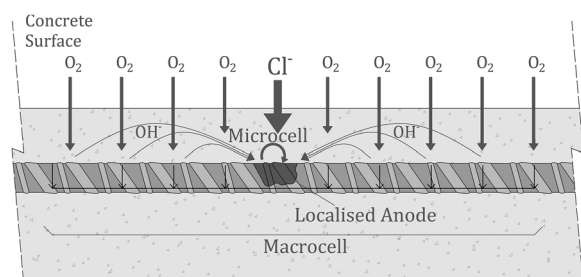Lliso-Ferrando *et al. Int J Concr Struct Mater*   (2023) 17:15

Page 2 of 17

size is and bigger its surrounding cathodic area is. This accepted logical statement has been demonstrated in several works (Andrade et al., 1992a, 1992b; Arya & Vassie, 1995). In the event of attacks occurring on rebars by pits, there is a tendency to believe that this region acts as a pure anode, although anodic and cathodic areas coexist in these regions (Bertolini et al., 1996; Evans, 1978; Mansfeld, 1971). The electric current generated at these points (microcells) is supported by a current that occurs between corroded and uncorroded areas (macrocell), a concept that is graphically depicted in Fig. 1 (Sangoju et al., 2011).

Macrocell currents have been experimentally studied by many authors. The main conclusions to be drawn from these works are: (1) the macrocell current is part of the total corrosion that a rebar undergoes. Macrocell corrosion can only be considered to be total corrosion when corrosion pit is very small or the corrosion cell occurs in fully de-aerated media (Andrade, 2019; Andrade et al., 2008); (2) macrocell currents are influenced by the position of rebars (cell configuration). In RCS, macrocells may be produced between parallel rebars, one in the active state and another in the passive state (face-to-face), or on the same rebar where anodic and cathodic areas co-exist (coplanar) (Elsener, 2002). Different studies have demonstrated that the face-to-face configuration contributes more to the corrosion rates of reinforcements than a coplanar arrangement does (Andrade et al., 1992a; Andrade et al., 1992b; Elsener, 2002; Raupach, 1996; Warkus et al., 2006; Warkus & Raupach, 2010); (3) concrete electrical resistivity plays a key role in macrocell current because it influences the cathodic surface that participates in these processes. The concrete types with higher electrical conductivity favour the circulation of ions which, thus, increases macrocell currents (Burkan-Isgor et al., 2009; Liu & Weyers, 1998; Pour-Ghaz et al., 2009);·(4) concrete's temperature and humidity impact not only the material's electrical resistivity, but also the kinetics of corrosion phenomena (Burkan-Isgor et al., 2009). Both these factors directly affect macrocell

processes;·(5) the cathode/anode surface ratio affects macrocell current. A bigger cathodic surface increases the demand for electrons in anodic areas and, therefore, a larger cathodic area implies greater macrocell current (Andrade et al., 2008; Belda et al., 2019; Gulikers, 1996).

Most of the aforementioned studies are limited to simulations of the concrete pore solution (Chen & Su, 2021; Dong & Poursaee, 2020), and sometimes to studies conducted with Standard Concrete (SC) (Belda et al., 2019). Very few authors have investigated macrocell currents in High-Performance Concrete (HPC). Hansson et al. (Hansson et al., 2006) found that macrocell currents in HPC were two orders of magnitude lower than those that could take place for the same case in SC. Jaffer and Hansson (Jaffer & Hansson, 2008) and Poursaee and Hansson (Poursaee & Hansson, 2009) observed that macrocell currents in HPC barely had any impact, not even under cracking conditions. No studies conducted with Very High-Performance Concrete (VHPC) or Ultra-High Performance Fibre-Reinforced Concrete (UHPFRC) (Serna et al., 2019; Yoo & Yoon, 2016) were found in the literature. These concrete types are characterised for having excellent mechanical capabilities and high durability thanks to a very dense porous structure (Valcuende et al., 2021a). This fact has led these materials being used in very aggressive environments, such as harbour areas or offshore platforms (European Union Funding for Research & Innovation, 2020; Lliso-Ferrando et al., 2019; Suesta et al., 2018). Although the benefits of these concretes have been well-studied from a mechanical point of view (Cadoni et al., 2019; Habel et al., 2006; Kang & Kim, 2012; Kang et al., 2010; Lim & Hong, 2016; Máca et al., 2013; Shafieifar et al., 2017; Shin et al., 2018; Wu et al., 2018; Zhang et al., 2018), their influence on corrosion phenomena, specifically on macrocell currents, has not been studied in-depth.

Bearing all this in mind, the main objective of this study was to contribute to existing works about modelling macrocell phenomena in RCS by focusing on the influence of the material's electrical resistance (R) and the limiting effect of the cathode/anode surfaces ratio. Its other objectives were to verify the influence of these parameters on macrocell phenomena and to demonstrate the difference between a study in solution and one in concrete. For this purpose, a study in solution was performed by means of electrochemical cells with different quality concretes (SC, HPC, VHPC and UHPFRC) as a porous membrane. Then, the same study was reproduced on rebars embedded in the different concretes, and the obtained results were compared to the solution studies.

Fig. 1 Outline of microcell and macrocell corrosion currents

Lliso-Ferrando *et al. Int J Concr Struct Mater*   (2023) 17:15

Page 3 of 17

2 Macrocell Currents in Reinforced Concrete

Macrocell currents in RCS occur because there are areas in rebars with a different chemical potential (Bertolini et al., 2013). Given the heterogeneity of the concrete and the steel employed in rebars, this phenomenon might materialise in between rebars in passive state, but its electric current is negligible because of the small electrochemical difference among elements. These currents intensify when depassivated rebar areas develop and come into electrical contact with areas that are still passive because a higher electrochemical gradient exists. Some examples of situations under these conditions are: (1) reinforcement in chloride-contaminated concrete in contact with reinforcements in chloride-free concrete (Bertolini et al., 2013; Cao et al., 2013; Chalhoub et al., 2020; Mir et al., 2019); (2) rebars affected by carbonation of concrete electrically connected to rebars in no carbonated concrete (Nasser et al., 2010); (3) corroding steel in old concrete comes into contact with reinforcements that are repassivated due to repairs (Christodoulou et al., 2013; Farzad et al., 2018; Qian et al., 2006; Ribeiro et al., 2013; Soleimani et al., 2010); (4) reinforcements affected by cracking that produce local rebar depassivation (Blunt et al., 2015; Firouzi & Rahai, 2013; Ji et al., 2016; Michel et al., 2013; Mohammed et al., 2001, 2003; Paul & van Zijl, 2017; Raupach, 1996; Shaikh, 2018; Subramaniam & Bi, 2010) or (5) electrically connected rebars with different Fermi levels, such as carbon steel bars and stainless steel bars (Dong & Poursaee, 2020; Pérez-Quiroz et al., 2008).

In order to theoretically study macrocell currents, it is necessary to firstly analyse the rebar areas in an active corrosion state and those in a passive state separately as if no electrical connection exists between them. If anodic (active corrosion steel) or cathodic (passivated steel) areas were analysed in microstructural terms, the state of each one would correspond to the sum of the anodic/cathodic semi-reactions that take place on their surfaces (François et al., 2018). The electrochemical polarisation behaviour of a single reversible electrode is usually modelled by Butler-Volmer equations. In this case, a rebar with active corrosion was considered (Eq. 1), as was a rebar in the passive state (Eq. 2). These equations are the summation of the corrosion currents in microstructural anodic and cathodic terms that take place in each system (Stern, 1957; Warkus & Raupach, 2006):

$$i_a = i_{corr}^a \cdot \left(e^{\frac{(E^a - E_{corr}^a)}{\beta_a^a}} - e^{\frac{-(E^a - E_{corr}^a)}{\beta_c^a}} \right) \tag{1}$$

$$i_p = i_{corr}^p \cdot \left(e^{\frac{(E^p - E_{corr}^p)}{\beta_a^p}} - e^{\frac{-(E^p - E_{corr}^p)}{\beta_c^p}} \right) \tag{2}$$

where i_a and i_p are the values of the net corrosion current that flows from the interface of a rebar with active corrosion and of a rebar under passivity conditions, respectively. The other parameters correspond to: i_{corr}^a and i_{corr}^p are the corrosion currents that take place on the surface of each rebar. Owing to their kinetic state, $i_{corr}^a >> i_{corr}^p$; E_{corr}^a and E_{corr}^p are the corrosion potentials of each rebar. Owing to their electrochemical state, $E_{corr}^a < E_{corr}^p$; E^a and E^p are the polarisation potentials for the corrosion potential of the rebar with active corrosion and the rebar in the passive state, respectively; values β_a and β_c refer to the coefficients of the anodic and cathodic Tafel slopes, respectively (Nasser et al., 2010).

Fig. 2 graphically represents the Eq. 1 and Eq. 2 for the two rebars electrically isolated and in different
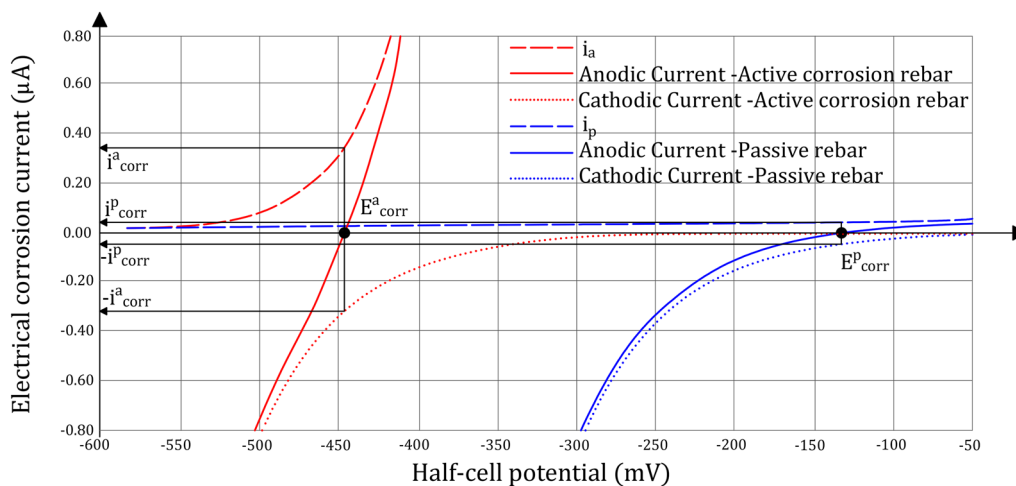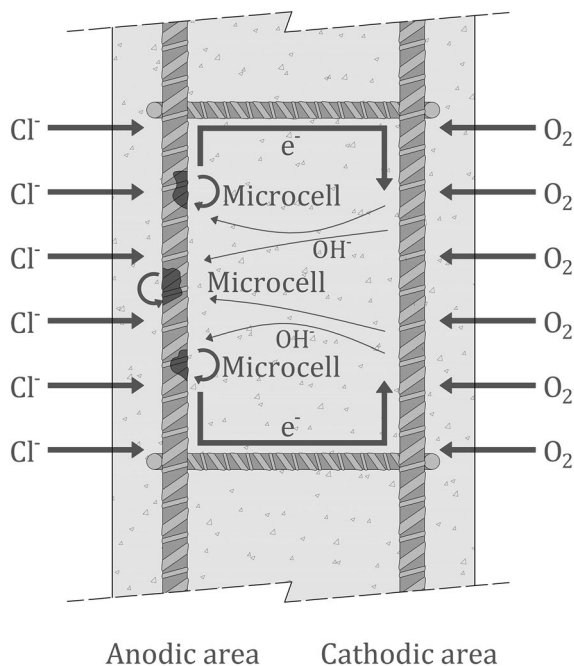

Fig. 2 Butler-Volmer diagram of the two isolated electrodes

Lliso-Ferrando *et al. Int J Concr Struct Mater*   (2023) 17:15

Page 4 of 17

electrochemical states: one under active corrosion conditions (red line) and another under passivity conditions (blue line). The value of the potentials E_{corr}^a and E_{corr}^p of each system corresponds to the point where corrosion currents are compensated (i_{corr}^a and i_{corr}^p). This means that an effective current flow cannot be observed under equilibrium conditions (François et al., 2018). Fig. 2 also shows the anodic/cathodic current intensities for each rebar (dashed/dotted lines).

Fig. 3 Electrically connected anodic and cathodic areas

That previously set out takes place microstructurally. However, in macrostructural terms, as electrically connected areas with different corrosion states co-exist, electrochemical cells are produced among these regions, which intensify corrosion currents because of a strong polarisation phenomenon (Nasser et al., 2010) (Fig. 3).

This process can be summarised as follows:·after electrically connecting the two previously described rebars with a different electrochemical potential, the metal with an active corrosion level and a more electronegative potential is polarised towards more positive potentials, which results in an apparent positive electric current (i_a).
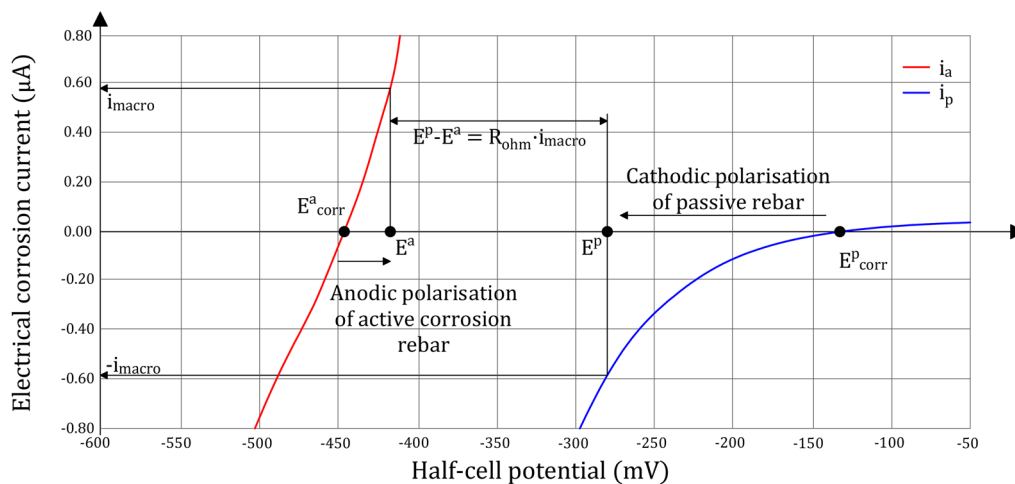
The region that is still in a passive state or with a more positive electrochemical potential is polarised after being electrically connected towards more negative potentials, which results in an apparent negative electric current (i_p). Both rebars do not reach an equilibrium point, but a difference in potential remains between them ($E^p - E^a$).

As a result of the connection, the system, which is now composed of two rebars, reaches an equilibrium as shown in Fig. 4. To reach this equilibrium, the system fulfils the two equations (Eq. 3 and Eq. 4):

$$i_a = -i_p = i_{macro} \tag{3}$$

$$E^p - E^a = R_{ohm} \cdot i_{macro} \tag{4}$$

where i_{macro} is the macrocell current between both electrodes and R_{ohm} corresponds to an ohmic drop, in this case concrete's resistance to ionic mobility. These two parameters comply with Ohm's Law and equal the difference in the electrodes' equilibrium potentials after polarisation.

Fig. 4 Butler-Volmer diagram of the two electrically connected electrodes

Lliso-Ferrando *et al. Int J Concr Struct Mater*   (2023) 17:15

Page 5 of 17

Table 1 Mixture proportions of concretes (kg/m³ concrete)

	C30	C40	C50	C90	UH-150
Cement: CEM II/B-M (V-LL) 32.5 N	307	–	–	–	–
Cement: CEM I 42.5 R/SR	–	292	450	500	800
Water	184	190	225	178	160
Superplasticizer Sika®-20HE	1.85	2.80	1.37	3.50	30
Silica fume	–	–	–	55	175
Silica flour	–	–	–	–	225
Siliceous sand fine (0/0.5)	–	–	–	–	302
Siliceous sand medium (0.6/1.2)	–	–	–	–	565
Limestone sand (0/4)	1438	1256	880	914	–
Limestone gravel (4/7)	–	–	880	779	–
Limestone gravel (4/12)	491	707	–	–	–
Steel fibres (Ø0.2mmx13mm)	–	–	–	–	175
w/b ratio	0.60	0.65	0.50	0.32	0.16

3 Experimental Plan

The experimental part of the present work involves studying the macrocell currents of rebars in simulated concrete pore solution and those embedded in concrete. These studies were performed with different concrete types and several cathode/anode surface ratios.

3.1 Materials

In order to analyse the macrocell currents in several concrete types, five mixes with different properties were prepared. The following types were made: low-strength concrete (C30), medium-strength concrete (C40), high-strength concrete (C50), very high-performance concrete (VHPC-C90) and ultra-high performance fibre-reinforced concrete (UHPFRC-UH150). The characteristics of each concrete mix appear in Table 1. All the concrete types were manufactured using CEM I 42.5 R/SR, except for concrete C30 for which cement CEM II/B-M (V-LL) 32.5 N was used. The chemical composition of the two cements and silica fume (SF) are depicted in Table 2.
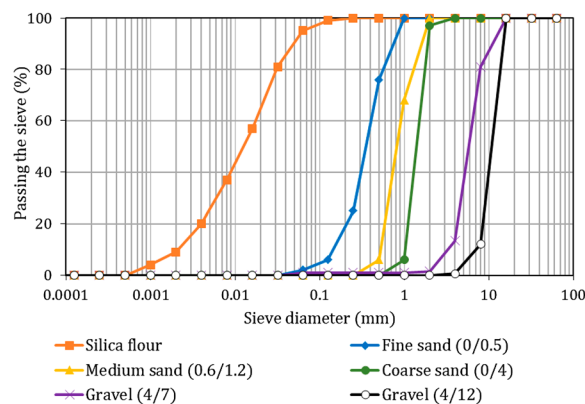

Fig. 5 Grading curves of silica flour, sands and gravels

Silica fume was included to produce concretes C90 and UH150. With concrete UH150, coarse aggregates were replaced with three silica sand types: a medium 0.6/1.2 one, a fine 0/0.5 one and silica flour of a similar particle size distribution to cement. Steel fibres were added in 2% (vol.) (Ø0.2 mm; 13 mm). The limestone aggregates for the other concretes consisted in 0/4 sand and 4/7 gravel. The density of aggregates is indicated in Table 3, and the grading curves of silica flour, sands and gravels are presented in Fig. 5.

The manufactured test specimens were stored in a curing chamber (20 °C and 95% RH) for 28 days. After this period, part of them was used to run a series of tests to characterise the materials. The results are provided in Table 4. These tests were run to determine:·(1) compressive strength (f_c) according to Standard UNE-EN 12,390–3:2009 (AENOR, 2009). This test was performed with three cylindrical specimens (Ø 100 mm; h = 200 mm) for each studied mixture;·(2) the porosity accessible to water according to Standard UNE 83980:2014 (AENOR, 2014). This test was performed

Table 2 Chemical composition of the cements and silica fume (in wt.%)

Cement	SiO₂	Al₂O₃	Fe₂O₃	CaO	MgO	SO₃	K₂O	Na₂O	LOI*	I**
CEM I 42.5 R/SR	20.16	5.12	2.62	63.87	1.62	3.03	0.65	0.23	2.12	0.58
CEM II/B-M (V-LL) 32.5 N	21.83	8.11	5.60	55.62	2.12	3.11	1.09	0.28	0.54	1.70
SF	86.64	1.65	1.39	2.68	2.66	0.18	–	1.35	2.67	–

* LOI: loss on ignition, **Insoluble

Table 3 Properties of aggregates

	Silica flour	Fine sand 0/0.5	Medium sand 0/2	Coarse sand 0/4	Gravel 4/7	Gravel 4/12
Density (g/dm³)	2.67	2.65	2.66	2.65	2.70	2.70

Lliso-Ferrando *et al. Int J Concr Struct Mater*   (2023) 17:15

Page 6 of 17

Table 4 Characterisation results

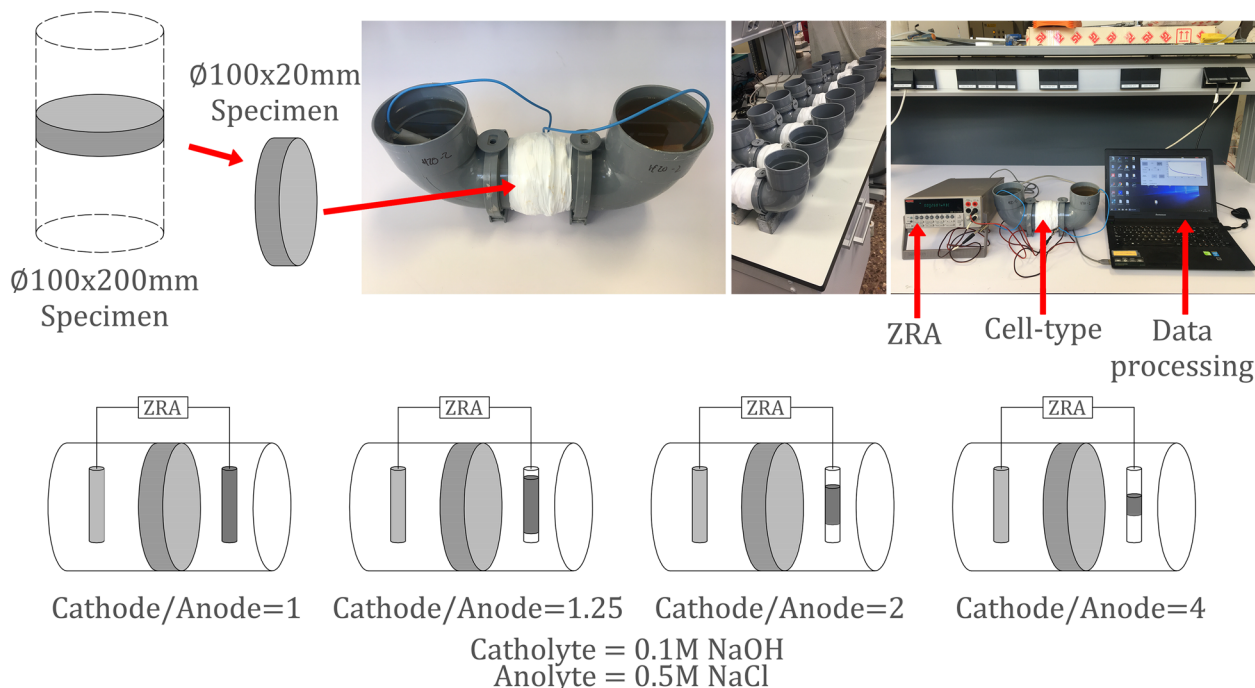|	C30	C40	C50	C90	UH-150
Compressive strength, f_c (MPa)	30.7 (1.12)	39.5 (0.99)	49.9 (0.32)	88.9 (1.96)	135.4 (2.01)
Water porosity (%)	18.5 (0.21)	17.2 (0.20)	14.8 (0.07)	9.1 (0.04)	1.9 (0.10)
D_{nssm} (m²/s)	$53.8 \cdot 10^{-12}$ ($4.1 \cdot 10^{-11}$)	$28.6 \cdot 10^{-12}$ ($1.5 \cdot 10^{-11}$)	$26.8 \cdot 10^{-12}$ ($8.5 \cdot 10^{-12}$)	$1.9 \cdot 10^{-12}$ ($1.3 \cdot 10^{-12}$)	$0.2 \cdot 10^{-12}$ ($1.3 \cdot 10^{-13}$)
Air permeability K_{gas} (m²)	$312.4 \cdot 10^{-18}$ ($8.3 \cdot 10^{-17}$)	$236.8 \cdot 10^{-18}$ ($2.3 \cdot 10^{-17}$)	$97.1 \cdot 10^{-18}$ ($2.8 \cdot 10^{-17}$)	$0.8 \cdot 10^{-18}$ ($2.3 \cdot 10^{-19}$)	$0.1 \cdot 10^{-18}$ ($4.9 \cdot 10^{-20}$)

Numbers in brackets are the coefficients of variation

with six prismatic specimens ($50 \times 100x100$ mm³) for each mixture;·(3) the non-steady-state migration coefficient (D_{nssm}), as set out in Standard NT Build-492 (NORDTEST, 1999). This test was performed with three cylindrical specimens (Ø 100 mm; h = 50 mm) for each mixture. The test provides a measure of concrete resistance to chlorides. A potential differential is applied to force the chloride migration through the concrete. Later, the specimens are axially split, and the inner faces are sprayed with 0.1 M $AgNO_3$ solution. The chloride-polluted area becomes whitish, and the penetration depth can be measured. The D_{nssm} coefficient is determined according to the expression set out in the standard;·(4) the air permeability coefficient (K_{gas}) according to Standard UNE 83981:2008 (AENOR, 2008). This test was performed with three cylindrical specimens (Ø 150 mm; h = 50 mm) for each mixture.

For the macrocell study, the following were produced for each concrete type:(1)·two specimens (Ø 100 mm; h = 200 mm) to manufacture cells with which to study macrocell currents in solution;·(2) six specimens (Ø50 mm, h = 100 mm) with embedded rebars. The following sections describe the assemblies in each study.

3.2 Cells To Study Macrocell Currents in Solution

In order to simulate a macrocell and to study how it behaved in solution, cells like those depicted in Fig. 6 were manufactured. Each cell was made up of two compartments separated by a porous membrane. This separation consisted in 20 mm-thick concrete discs (Ø 100 mm), which were obtained from the central part of cylinders (Ø 100 mm, h = 200 mm) by a saw-cut and were made with the concretes specified in the previous section. The lateral disc side was sealed with epoxy resin

Fig. 6 Diagram showing the cells and the macrocell configuration

and TeflonTM tape. Two cells were produced for each studied concrete type.

Steel B 500 SD is commonly used in reinforced concrete structures. To simulate the behaviour of a real structure and to generate a macrocell current between its different regions, a decision was made to use this type of steel in the anodic zone and high-quality steel in the cathodic zone, which would remain under passive state throughout the test period (stainless steel AISI 304). In AISI 304, given its high chromium content, a very stable passivating oxide layer is formed which prevents steel oxidation.
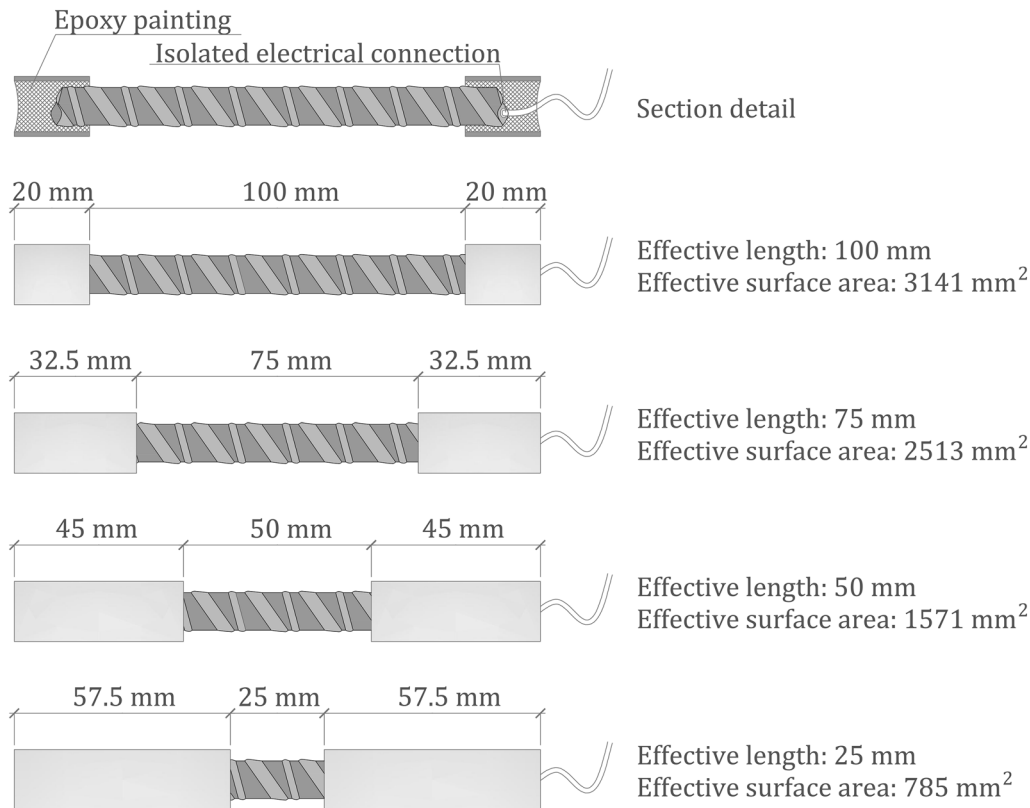
Accordingly, in each cathodic compartment, a stainless steel (AISI 304; Ø 10 mm, 120 mm length) rebar was immersed. Rebar ends were protected with PVC pipe filled with epoxy resin. The length of the rebar in contact with the solution was 100 mm (effective surface area 3141 mm^2). In anodic compartments, the segments of rebar B 500 SD (Ø 10 mm, 120 mm length) were used. The rebars' surface in contact with solution was also delimitated using PVC protection filled with epoxy resin on rebar ends. In this case, protections of different sizes were used (Fig. 7). This strategy allowed rebars to be achieved with different effective lengths: 100, 75, 50

Table 5 Cathode/anode configuration

S$_c$/S$_a$ (cathode/anode surface ratio)	1	1.25	2	4
Cathode surface (mm^2)-S$_c$ [stainless steel]	3141	3141	3141	3141
Anode surface (mm^2)-S$_a$ [carbon steel]	3141	2355	1571	785

and 25 mm (effective surface areas: 3141, 2355, 1571 and 785 mm^2, respectively). The effective surface areas and the cathode/anode surface ratio analysed in each case are presented in Table 5. The chemical composition of the two steels and their mechanical properties appear in Tables 6 and 7, respectively. To simulate different alkalinities and to generate macrocells, 0.5 M *NaCl* solution was employed to intensify the anodic behaviour of the carbon steel rebar in solution by bringing about the metal's depassivation and, therefore, favouring active corrosion processes to take place in it. On the other hand, in the cathodic compartment, 0.1 M *NaOH* solution was used to emphasise the cathodic character of the stainless steel in the system.

Other authors have used this type of cells to analyse macrocells, and it is typical in diffusion experiments (Andrade, 2019; Andrade et al., 1992a, 2008; Chen & Su,

Fig. 7 Rebars used in this study

Table 6 Chemical composition of the steels (in wt.%, balance Fe)

Steel	C	Si	Mn	S	Cr	Ni	Cu	N	Mo	Ti
AISI304	0.023	0.38	1.49	0.022	18.55	8.77	0.176	0.18	0.21	0.003
B500 SD	0.19	0.24	0.95	0.025	0.11	0.13	0.34	–	0.02	–

Table 7 Mechanical properties of the steels

Steel	fy (MPa)	fs (MPa)	E (MPa)	εu (%)
AISI304	442	745	173000	48
B500 SD	555	681	216000	24

fy: yield strength, fs: ultimate tensile strength, E: modulus of elasticity, εu: failure tensile strain

2021; Dong & Poursaee, 2020). Andrade et al. (Andrade et al., 2008) used discs of a few millimetres (3 mm) and Chen et al. (Chen & Su, 2021) employed 10 mm thick discs. In this case, 20 mm discs were utilised because cracks or faults might appear with narrower discs, which could cross the whole part's section and lead to misinterpretations.

All the configurations described in Table 5 were analysed for 2 weeks. In order to do this, each pair of rebars was submerged in solution and was left electrically connected for 7 days for the depassivation of the carbon steel reinforcements (see Fig. 6). As metal pieces were submerged in different electrochemical environments, an electrochemical cell was generated and macrocell currents were induced. After this time, measurements were taken of the electric currents generated between the rebars of each compartment every 24 h. This measurement was taken by a Zero Resistance Ammeter (ZRA), model Keithley 2000 Tektronix. The value was recorded 5 min after measurements began to ensure that the recorded signal was stable enough. The obtained value was normalised by the rebar surface of the anodic compartment rebar to obtain the macrocell current density (j_{macro}).

Another analysed parameter was the cell's electrical resistance, which was defined as the inverse of the conductance measured between two electrodes. Measurements were taken with a commercial conductivity meter (CRISON GLP-32), which was connected to the two bars that were immersed in the cell: one in the cathodic compartment (catholyte) and the other one in the anodic compartment (anolyte). The value was recorded 2 min after measurements began to ensure that the recorded signal was stable enough. The total electrical resistance of the cell is the sum of three resistances: the catholyte, the anolyte and the porous membrane (concrete disc).

The uniformity of the distribution of the electric field lines between the electrodes in the cell is affected by the geometry and size of the concrete disc and electrodes, the distance between electrodes, and also the materials' resistivity (Andrade et al., 1992b; Bataller-Prats et al., 2015). In this experimental work the electrodes were immersed in an aqueous medium and each at sufficient distance from the concrete disc (130 mm) to accept that the electric field aperture was maximum and equalled the concrete disc's diameter (Gandía-Romero et al., 2017). Therefore, considering that the solutions used in the cell are highly conductive (0.5 M *NaCl* and 0.1 M *NaOH*), the following linear relation can be assumed:

$$R_T = \frac{l}{S_c} \cdot \rho \quad (5)$$

where S_c is the concrete disc's cross section and l is the distance between the electrodes used to take the measurement ($S_c = 78.5$ mm^2 and $l = 20$ mm).

Throughout the process, the alkalinity of solutions was controlled. To do so, the pH in each cell compartment was measured by a pH-meter, model CRISON GLP-22. Due to the observed changes, the solution in tanks was changed every two weeks so that the conditions in all the tests would be similar.
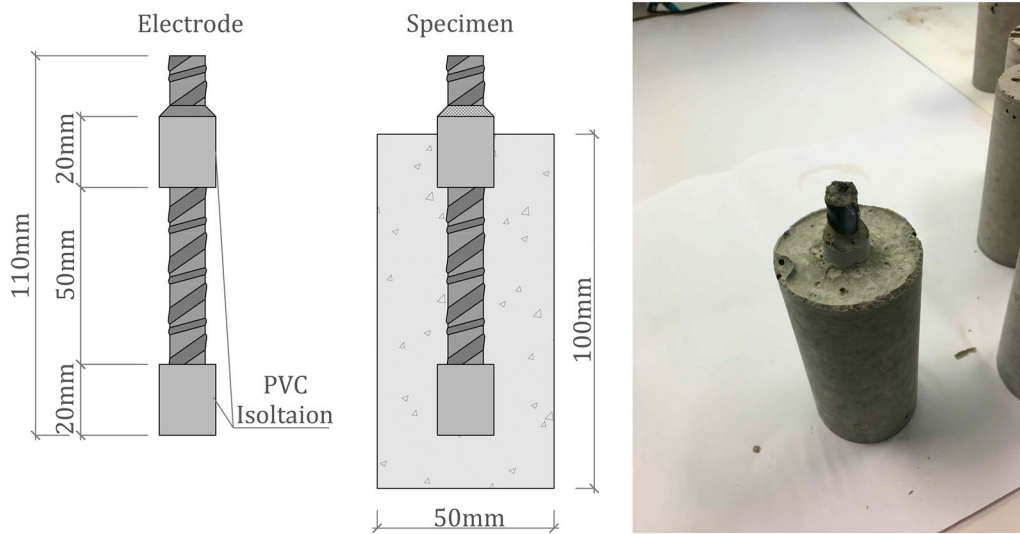
3.3 Study of the Macrocell Currents in Concrete

After the solution study, the macrocell currents in concrete were studied. The experimental plan was devised by considering the same study parameters: the concrete's electrical resistance and the cathode/anode surface ratio.

In order to accelerate the corrosion process of the reinforcement, a decision was made to use specimens in which the concrete cover was not large. In this way, macrocell currents were also favoured because the ionic current through the concrete cover decreases as the concrete cover increases. For this purpose, and using the concrete mixes described in Sect. 3.1 cylindrical test specimens were manufactured (50 mm in diameter, 100 mm high) with a rebar (B500 SD) inserted into the centre. The concrete cover was 20 mm (Fig. 8).

Six specimens were manufactured for each concrete mix. After 28 curing days, they were divided into two groups: (A) three specimens were partially submerged (up to 80 mm) in 0.1 M *NaOH* solution; (B) three
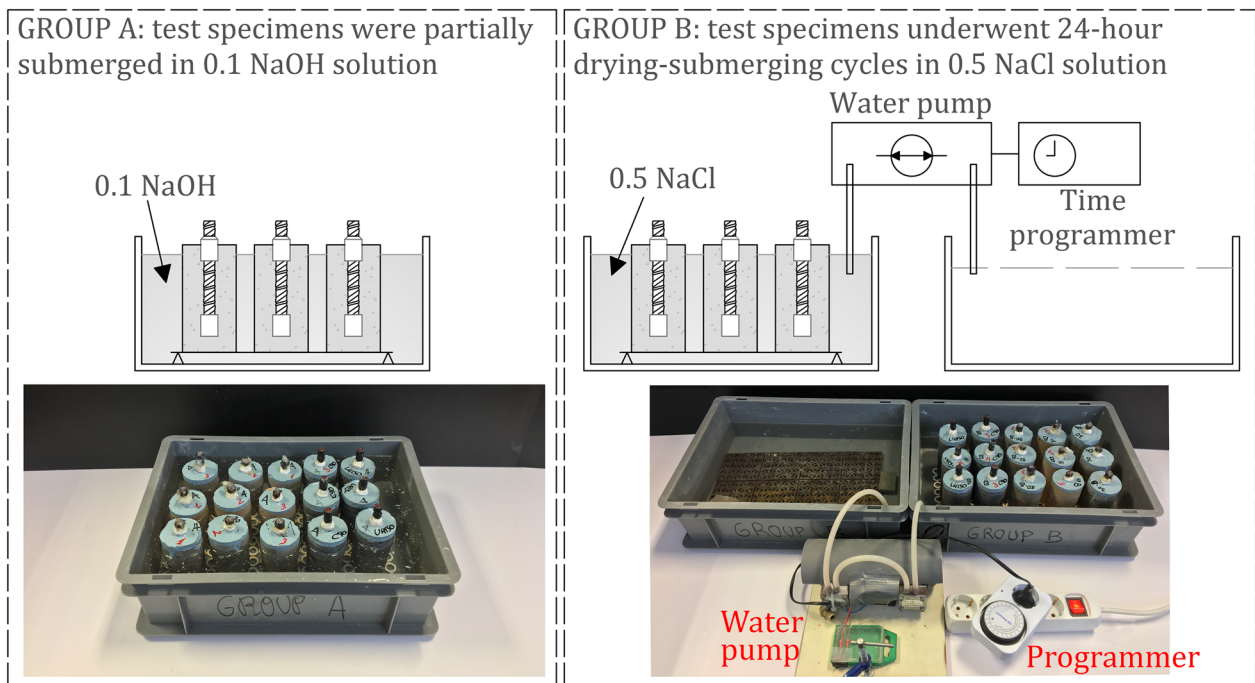
Fig. 8 Test specimens from the study of the macrocell currents in the rebars embedded in concrete

specimens underwent 24 h drying-submerging cycles in 0.5 M *NaCl* solution to ensure that chlorides had diffused in the cementitious matrix. A water pump and a commercial time programmer were used to generate dry–wet cycles. In both groups, the specimens were left under these conditions for 6 months. Two diagrams and pictures of the setup of tests are shown in Fig. 9.

This allowed rebars to be obtained under different electrochemical conditions for all the used concrete types: some in the passive state (those left in 0.1 M *NaOH* solution) and others in the active state, with corrosion showing as a result of chloride attacks.

These rebars' corrosion current was periodically measured while the 6-month exposure lasted by the linear polarisation resistance (LPR) technique described in
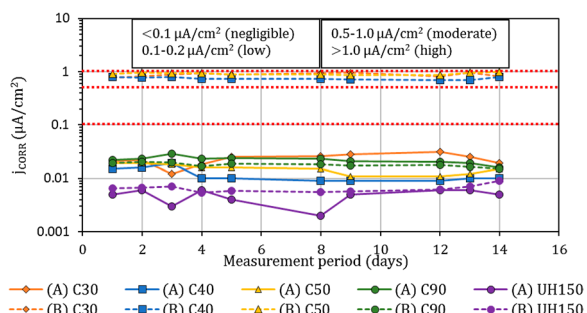

Fig. 9 Setup of the exposure conditions

UNE 112072 (AENOR, 2011). After this time, the specimens in group (A) still had a negligible corrosion level (< 0.10 µA/cm^2) and those in group (B) had a moderate-high corrosion level (> 0.50 µA/cm^2) according to the ranges set out in the RILEM TC 154-EMC recommendations (Andrade et al., 2004).

When this 6 month period ended, specimens were left submerged in the exposure solution for 2 more weeks, during which time they were monitored to assess rebars' corrosion. The average values of each group obtained during the monitoring period in the last fortnight are found in Fig. 10. In line with Andrade et al. (Andrade et al., 2004), checks were made to see if the specimens in group (B) presented a moderate corrosion level, which came very close to a high degree, while the specimens in group (A) remained in the passive state. In this latter group, the corrosion rate values in the five concretes were negligible, with no significant differences between them.
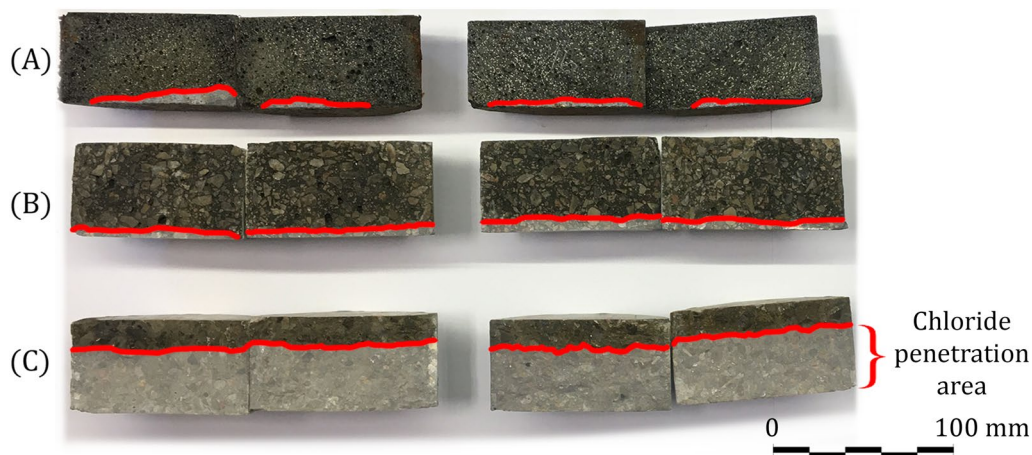
According to the results presented in Fig. 10, the specimens made with concretes C90 and UH150 of group B were not considered because the embedded rebars

remained under passive state after undergoing submerging-drying cycles in solution with chlorides for 6 months. In these concretes, the exposure was extended for 6 more months and the obtained corrosion values were still negligible (Lliso-Ferrando, 2022). Chloride diffusion in these concrete matrices was practically null, as proven by the results obtained for the accelerated chloride migration testing NT Build-492 (NORDTEST, 1999) and presented in Table 4, where the chloride migration coefficient from the non-steady-state migration (D_{nssm}) was much lower in these concretes. Some authors have also proved this statement, even under cracking conditions (Mafalda et al., 2021; Matos et al., 2020). Fig. 11 depicts chloride penetration depth, marked with the whitish colour after being sprayed with 0.1 M $AgNo_3$ solution. For concrete UH150, this penetration was almost non-perceptible, it was 2–3 mm for C90 and around 40 mm for C40.
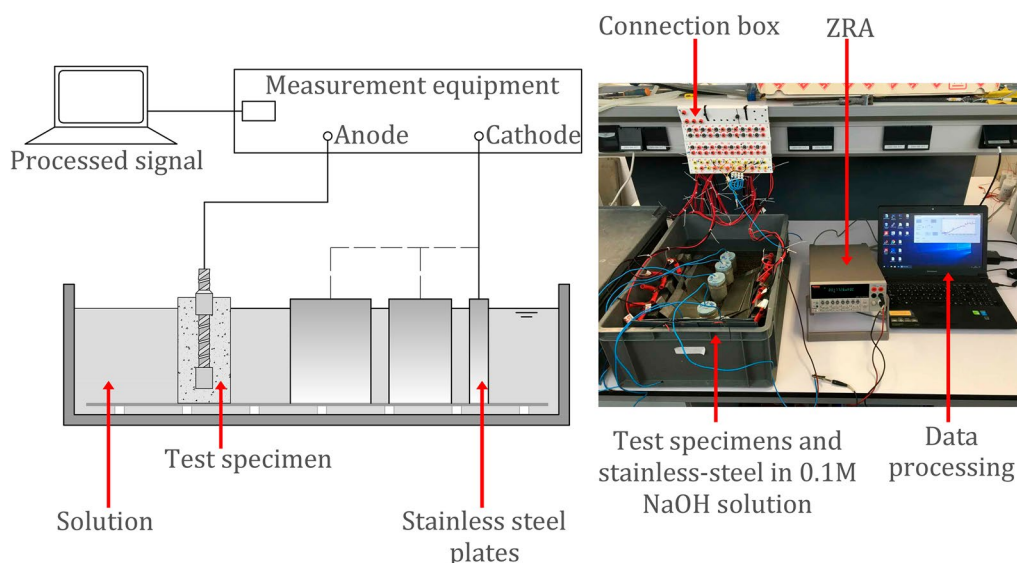
After the 6-month exposure period, the macrocell currents analysis was carried out with the different test specimens in two tanks under the same solutions in which they were submerged during the exposure process: 0.1 M *NaOH* for the rebar specimens in the passive state (A); 0.5 M *NaCl* for those affected by the presence of chlorides (B). In each tank, stainless steel pieces were placed (Fig. 12) to act as cathodes. The analysed cathode/anode surface ratios were the same studied in Sect. 3.2 for rebars in solution: Sc/Sa = 1, 1.25, 2 and 4. To obtain these ratios, the effective surface of the steel plates was 1571, 1963, 3142 and 6284 mm^2, respectively. A ZRA model Keithley 2000-Tektronix was used to measure the macrocell current. The value was recorded 10 min after measurements began to ensure that the recorded signal was stable enough. The obtained macrocell current value (i_{macro}) was normalised by the rebar surface to obtain the macrocell current density (j_{macro}).

Fig. 10 Corrosion density currents for the 14-day corrosion monitoring period

Fig. 11 Comparison of the chloride diffusion test. (A) UH150; (B) C90; (C) C40

Fig. 12 Studying the macrocell currents in the concrete specimens

Later, the macrocell currents were analysed for 21 other cathode/anode surface ratios (7.5, 15, 20, 25, 30, 40, 45, 50, 75, 100, 130, 150, 180, 200, 230, 270, 315, 350, 385, 410, 450). For this purpose, the rebars (anode) were connected to some stainless steel plates with larger surfaces (from 11782 mm^2 to 708000 mm^2). Some diagrams and pictures of this experimental are presented in Figs. 12 and 13.

4 Results and Discussion
4.1 Solution Studies
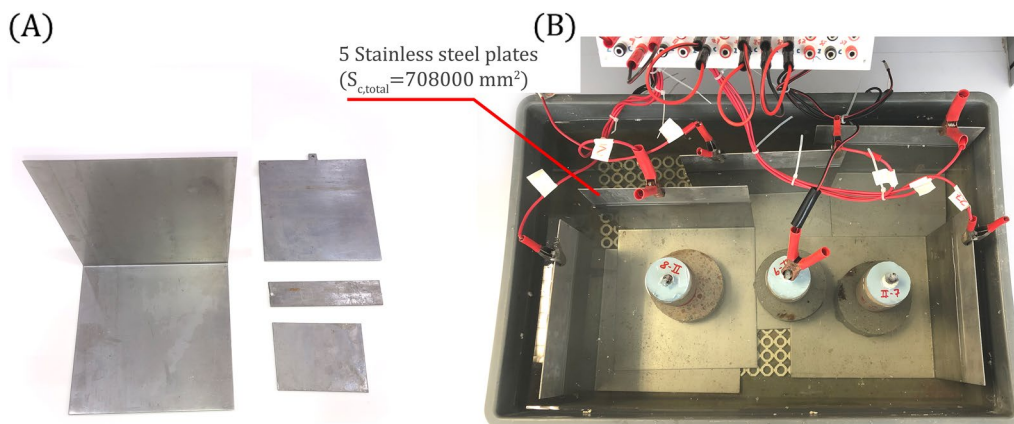#### *4.1.1 Effect of Resistivity On Macrocell Currents*
Macrocell current density (j_{macro}) and concretes' electrical resistance (R) obtained for the cathode/anode surface ratio equal 1 are presented in Table 8. This table includes the coefficients of variation (number in brackets).

Fig. 14 correlates the values in Table 8 by detecting an inverse correlation between the macrocell current density (j_{macro}) and the concrete's electrical resistance (R). In other words, the lower the concrete's resistance is, the higher the current density is.

The results obtained in samples C30 showed 20% higher macrocell intensity values than C40. The difference between concrete C40 and concrete C50 was only 5%. C90 and UH150 presented lower macrocell current density than the other concrete types.

In ultra-high performance fibre-reinforced concretes, such as UH150, the steel fibres present in the mix increased the concrete's conductivity because steel
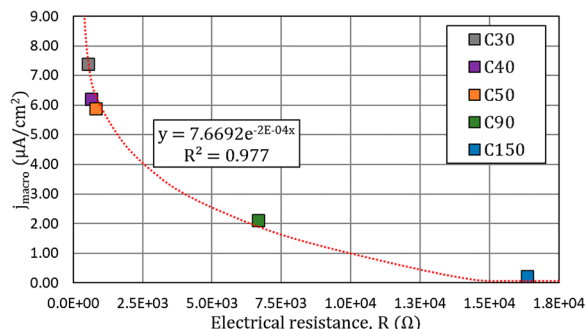

Fig. 13 Detail of the macrocell study: (**A**) stainless steel plates with different surfaces to obtain different Sc/Sa ratios and (**B**) setup for Sc/Sa = 450

Lliso-Ferrando *et al. Int J Concr Struct Mater*   (2023) 17:15

Page 12 of 17

Table 8 Macrocell current density (j_{macro}) and concrete's electrical resistance (R) for the cathode/anode surfaces ratio 1

	C30	C40	C50	C90	UH-150
Macrocell current density, j_{macro} ($\mu A/cm^2$)	7.39 (0.51)	6.20 (0.78)	5.89 (0.82)	2.12 (0.11)	0.22 (0.02)
Concrete's electrical resistance, R (Ω)	536.53 (60.62)	651.99 (64.64)	801.02 (116.16)	663.85 (160.09)	16362.6 (349.83)

Numbers in brackets are the coefficients of variation

Fig. 14 Correlation between j_{macro} and concrete's electrical resistance, R for Sc/Sa = 1

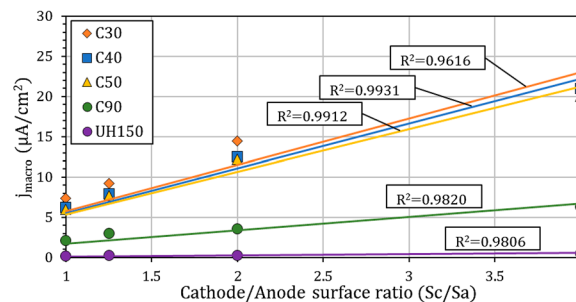**Fig. 15** Correlation (j_{macro} vs. Cs/As) in solution

possesses negligible resistance to electrons' movement (Valcuende et al., 2021a). Nevertheless, these concretes are characterised by having a very dense porous structure (Scheydt & Muller, 2012; Valcuende et al., 2021b) and, consequently, very high resistivity. In fact, although steel fibres reduce resistivity, UH150 electrical resistance was nearly threefold greater than concrete C90 (Lliso-Ferrando, 2022). This higher resistance limits the ionic current in concrete, which decreases the macrocell current, and the j_{macro} value obtained in UH150 was one order of magnitude lower than in C90.

These data reflect the impact that these concrete types had on macrocell currents: a much denser structure and a porous network with more tortuosity would make them less permeable, which means that the resistance to ion circulation in the porous material was much greater.

4.1.2 Effect of the Cathode/Anode Surface Ratio
Fig. 15 provides the average values obtained from the 2 weeks monitoring of all the described configurations in Table 5. This figure also indicates the correlation between j_{macro} and the cathode/anode surface (Cs/As) ratio.

Macrocell current density (Fig. 15) varies according to the surface's ratio. Lower macrocell densities are obtained for a Cs/As ratio equalling 1. However, if this ratio rises, the electrons demand for the same anode surface increases because of a larger cathodic surface where the reduction reaction occurs. The difference between configurations Cs/As 4 and 1 might vary by 400% for
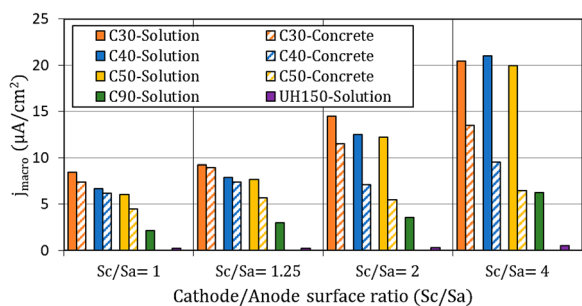
conventional concrete types. This increase in concrete types C90 and UH150 was lower (100%) due to the limitation imposed by the material's electrical resistance (*R*). The obtained results also show a direct linear correlation between j_{macro} and the Cs/As ratio. The average R^2 was beyond 0.96 in all cases (C30 = 0.9616; C40 = 0.9931; C50 = 0.9912; C90 = 0.9820; UH150 = 0.9806). The slopes of concrete types C30, C40 and C50 were similar (5.3–5.7 $\mu A/cm^2$). However, the slope in C90 was (1.69 $\mu A/cm^2$) and was negligible in UH150 (0.14 $\mu A/cm^2$), which indicates that transport phenomena would be very limited. Thus, regardless of how much bigger the cathode surface could be, the macrocell would not produce a field with enough current to considerably increase the electric charge flow through the dielectric material (concrete). The solution study allowed to simply and quickly check the influence of the concretes' electrical resistance and the Cs/As ratio in the macrocell currents.

4.2 Study in Concrete
4.2.1 Differences From Studies in Solution
In order to evaluate the limitations of the macrocell currents analysis performed in solution, the previous testing was replicated, but by using the rebars embedded in concrete in this case. For this purpose, the reinforced concrete specimens from group (B) described in Sect. 3.3 were used, which had been exposed to chloride action and showed high corrosion levels because of their depassivation (only concrete types C30, C40 and C50). Fig. 16

Fig. 16 Macrocell current density in solution and in the rebars embedded in concrete
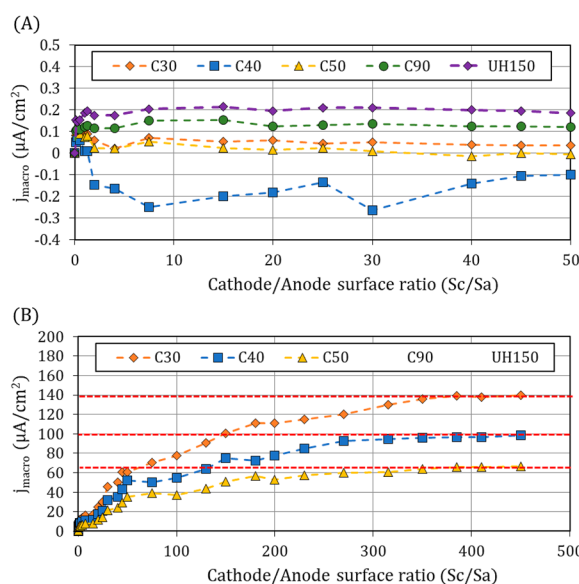
compares the values obtained in solution and those in concrete for the same Cs/As ratios.

Fig. 16 shows how the macrocell corrosion current is lower in the rebars embedded in concrete and, the bigger the differences are, the higher the Cs/As ratio is. For example, the difference between j_{macro} in solution and in concrete C30 for a Cs/As ratio of 1 is 14%, while this difference is 42% for a Cs/As ratio of 4. This phenomenon is because of the ohmic drop effect, which is much stronger when rebars are directly embedded in concrete. When rebars are in solution (aqueous medium), the oxides that generate on the surface of the metal diffuse rapidly into solution. However, when rebars are embedded in concrete, oxides do not pass directly to the pore solution, but are retained on the rebar's surface, which prevents rapid diffusion of the generated products. As a result, the oxides layer reduces macrocell processes. Because of this, the tests in which the macrocell current was studied on the rebars in solution led to overestimate them. In fact some authors (Duffó & Farina, 2016) have reported that studies in solution can be useful, but extrapolation to behaviour in concrete is not adequate.

4.2.2 Macrocell Currents in the Rebars Embedded in Concrete

The impact that the cathode area had on the macrocell currents of the rebars embedded in concrete was assessed in both test specimens: group (A) and group (B). To do this, the configuration Cs/As ratio was progressively increased until j_{macro} reached a stable value (Fig. 17). In group B specimens C90 and UH150 were not considered because rebars did not reach the depassivation condition after 6 months of exposure.
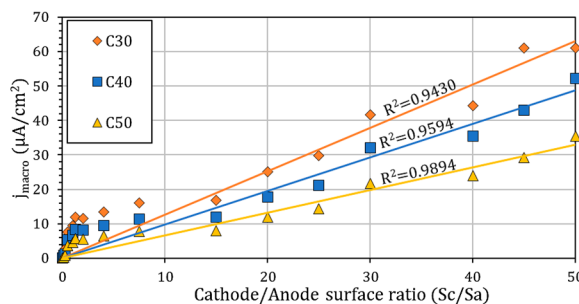
Fig. 17A shows that when rebars were in the passive state, j_{macro} was negligible and remained constant over time owing to the similarity of the electrochemical state of both the rebars and the stainless-steel elements submerged in 0.1 M *NaOH* solution. This finding reveals that the macrocell currents among the elements in the passive state do not affect the structure's durability.

Fig. 17 Progress of the macrocell current at different cathode/anode ratios for the different concrete types: (**A**) passive state; (**B**) active state. *C90 and UH150 in group (**B**) were not considered

For the rebars in the active state (group B) (Fig. 17B), it is worth firstly stressing that for up to a Cs/As ratio of 50, the graphs present a straight-lined stretch for the three concrete types (Fig. 18), where the R^2 value is always above 0.94. In this stretch, j_{macro} and the Cs/As ratio are linearly correlated, and the higher the Cs/As ratio is, the higher j_{macro} becomes. In the solution study, this linear correlation was also found, but with a difference in the slopes of concrete types C30, C40 and C50 which was almost negligible (Fig. 15). In this case, when the rebars were embedded in concrete, the electric charge transport was much more limited and the differences between the three concretes were more noticeable.

For Cs/As ratios over 50 (Fig. 17B) the slope decreases, and the values tend to stabilise by reaching constant rates

Fig. 18 Evolution of the macrocell current between Cs/As = 1 and Cs/As = 50

Lliso-Ferrando *et al. Int J Concr Struct Mater*   (2023) 17:15

Page 14 of 17

for Cs/As ratios of around 400. Values were considered stable when the coefficient of variation between two consecutive measurements was below or equalled 1%.
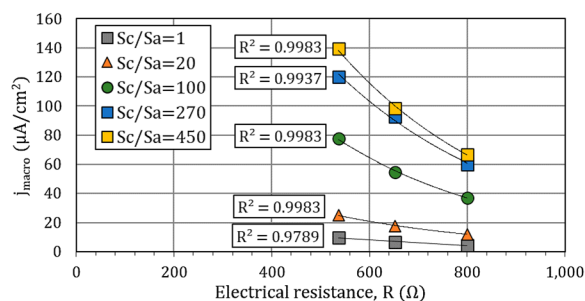
These variations in the curves' morphology were due to changes in the phenomena that controlled the macrocell process. The first curve stretch, which was linear, was controlled by the concrete's electrical resistance (different slopes among the concrete types) and the cathode surface (the bigger its surface, the higher the j_{macro} value). For the second curve stretch, the macrocell phenomenon was governed by the anode's electronic transfer and the field intensity generated in the macrocell, which depend on the concrete's electrical resistivity and condition the limit value that was reached. The obtained results showed that this limit was reached earlier in the concrete types with higher resistivity because the produced macrocell was unable to move more electric charge given the polarisation between the anode and cathode.

These results demonstrated that the anode had a limit value in each case from which no more electrons could be transferred because the limit of the field intensity generated between the two poles of the created macrocell had been reached. The difference between the limits for each concrete type indicated that the electrical resistance of the media also influenced this aspect. For greater electrical resistance, the limitation would occur earlier because ions would need more energy to cover the distance between macrocell poles.

Achieving the cathode/anode surface ratio described above (Sc/Sa beyond 400) is very unlikely in real structures and could only occur in zones with a high reinforcements' density and a very localised anode. Under normal conditions, the macrocell phenomena intensity is strongly conditioned by the electron's demand exerted on the anodic region, which is regulated by the cathode surface that participates in the process. In turn, the amount of cathodic surface participating in the macrocell is determined by the concrete's resistivity. Thus, concrete resistivity governs the internal macrocell processes in reinforced concrete structures. In addition, and as reported in the solution study, an inverse correlation appears between the macrocell current density and the concretes' electrical resistance (Fig. 19).

5 Conclusions

Based on the experimental results obtained with the solution study, it was possible to verify that: (1) the employed cell configuration is ideal for quick macrocell phenomena studies in solution. This configuration allows the analysis of different cathode/anode configurations with distinct concrete discs employed as separations. For future works, it allows the used electrolyte to be modified, which extends the possibilities of this study; (2) the

Fig. 19 Correlation between macrocell current density (j_{macro}) and concretes' electrical resistance (R)

study done with these cells demonstrates the influence of both the Cs/As ratio and concrete's electrical resistance on macrocell currents; (3) the improvement achieved using concrete types VHPC and UHPFRC in macrocell currents is proved. Their structures are much less permeable, which significantly reduces ionic mobility and implies much lower macrocell currents compared to identical configurations, but with conventional concrete types. To date, no tests have been performed to analyse the macrocell effect on these concrete types by means of this configuration.

The analysis of the macrocell currents in the rebars embedded in reinforced concrete demonstrated: (1) the large difference in the results compared to the studies in solution. This fact proves that studies in solution do not completely represent the reality when rebars are embedded in concrete. The theoretical study of macrocells in solution might be interesting to quickly and simply analyse different parameters, but the obtained results must not be interpreted as the reality of RCS; (2) the Cs/As ratio plays a key role in regulating macrocell current intensity. However, what really governs this phenomenon is concrete's R, which conditions the participation of a bigger or smaller cathode surface which, in turn, regulates the macrocell currents. Therefore, macrocells are under ohmic control.

Author contributions
JRLF and MV devised the main conceptual idea, performed the formal analysis, evaluated the results and contributed to draft the script. IG and AMI supervised the work and made critical comments about this manuscript. All the authors discussed and contributed to the final manuscript. All the authors read and approved the final manuscript.

Lliso-Ferrando *et al. Int J Concr Struct Mater*   (2023) 17:15

Page 15 of 17

Authors' information
Josep Ramon Lliso-Ferrando*, Ph.D. Architect, Research Institute for Molecular Recognition and Technological Development (IDM), Electrochemistry Laboratory, 1B-ETSIE, Universitat Politècnica de València, Camino de Vera, s/n., 46022 Valencia, Spain.
Isabel Gasch, Ph.D. Design Engineer & Professor, Research Institute for Molecular Recognition and Technological Development (IDM), Electrochemistry Laboratory, 1B-ETSIE, Universitat Politècnica de València, Camino de Vera, s/n., 46022 Valencia, Spain.
Ana Martínez-Ibernón, Ph.D. Architect & Professor, Research Institute for Molecular Recognition and Technological Development (IDM), Electrochemistry Laboratory, 1B-ETSIE, Universitat Politècnica de València, Camino de Vera, s/n., 46022 Valencia, Spain.
Manuel Valcuende, Ph.D. Student, Building Engineer, Department of Architectural Constructions, Electrochemistry Laboratory, 1B-ETSIE, Universitat Politècnica de València, Camino de Vera, s/n., 46022 Valencia, Spain.

Availability of data and materials
The datasets used and/or analysed in the present study are available from the corresponding author upon reasonable request.

Declarations

Competing interests
The authors declare that they have no competing interests.

References
AENOR. (2008). *UNE-EN 83981. Determinación de la permeabilidad al oxígeno del hormigón endurecido*

AENOR. (2009). *UNE-EN 12390–3. Ensayos de hormigón endurecido. Parte 3: Determianción de la resistencia a compresión de probetas. UNE-EN*

AENOR. (2011). *UNE 112072. Determinación de la velocidad de corrosión de armaduras en laboratorio mediante medida de la resistencia a la polarización*

AENOR. (2014). *UNE-EN 83980. Determinación de la absorción de agua, la densidad y la porosidad accesible al agua del hormigón*

Alonso, C., Andrade, C., Castellote, M., & Castro, P. (2000). Chloride threshold values to depassivate reinforcing bars embedded in a standardized OPC mortar. *Cement and Concrete Research, 30*(7), 1047–1055. https://doi.org/10.1016/S0008-8846(00)00265-9

Altoubat, S., Maalej, M., & Shaikh, F. U. A. (2016). Laboratory Simulation of Corrosion Damage in Reinforced Concrete. *International Journal of Concrete Structures and Materials, 10*(3), 383–391. https://doi.org/10.1007/s40069-016-0138-7

Andrade, C., Maribona, I. R., Feliu, S., & Gonzalez, J. A. (1992a). Macrocell Versus Microcell Corrosion of Reinforcement Placed in Parallel. *Annual Conference and Corrosion Show*

Andrade, C. (2019). Propagation of reinforcement corrosion: Principles, testing and modelling. *Materials and Structures, 52*(1), 1–26. https://doi.org/10.1617/s11527-018-1301-1

Andrade, C., Alonso, C., Gulikers, J., Polder, R., Cigna, R., Vennesland, S. M., Raharinaivo, A., & Elsener, B. (2004). RILEM TC 154-EMC: "electrochemical techniques for measuring metallic corrosion". test methods for on-site corrosion rate measurement of steel reinforcement in concrete by means of the polarization resistance method. *Materials and Structures/materiaux Et Constructions., 37*(273), 623–643. https://doi.org/10.1617/13952

Andrade, C., Garcés, P., & Martínez, I. (2008). Galvanic currents and corrosion rates of reinforcements measured in cells simulating different pitting areas caused by chloride attack in sodium hydroxide. *Corrosion Science, 50*(10), 2959–2964. https://doi.org/10.1016/j.corsci.2008.07.013

Andrade, C., Maribona, I. R., Feliu, S., González, J. A., & Feliu, S. (1992b). The effect of macrocells between active and passive areas of steel reinforcements. *Corrosion Science, 33*(2), 237–249. https://doi.org/10.1016/0010-938X(92)90148-V

Angst, U., Elsener, B., Larsen, C. K., & Vennesland, Ø. (2009). Critical chloride content in reinforced concrete—A review. *Cement and Concrete Research, 39*(12), 1122–1138. https://doi.org/10.1016/j.cemconres.2009.08.006

Angst, U., Elsener, B., Larsen, C. K., & Vennesland, Ø. (2011). Chloride induced reinforcement corrosion: rate limiting step of early pitting corrosion. *Electrochimica Acta, 56*(17), 5877–5889. https://doi.org/10.1016/j.electacta.2011.04.124

Arya, C., & Vassie, P. R. W. (1995). Influence of cathode-to-anode area ratio and separation distance on galvanic corrosion currents of steel in concrete containing chlorides. *Cement and Concrete Research., 25*(5), 989–998.

Ayinde, O. O., Zuo, X. B., & Yin, G. J. (2019). Numerical analysis of concrete degradation due to chloride-induced steel corrosion. *Advances in Concrete Construction, 7*(4), 203–210. https://doi.org/10.12989/acc.2019.7.4.203

Bataller-Prats, R., Gandía-Romero, J. M., García-Breijo, E., Alcañiz, M., & Soto, J. (2015). A study of the importance of the cell geometry in non-faradaic systems a new definition of the cell constant for conductivity measurement. *Electrochemica Acta2, 153*(20), 263–272. https://doi.org/10.1016/j.electacta.2014.12.014

Behera, P. K., Moon, A. P. K., Mondal, K., & Misra, S. (2016). Estimating critical corrosion for initiation of longitudinal cracks in RC structures considering phases and composition of corrosion products. *Journal of Materials in Civil Engineering, 28*(12), 04016158. https://doi.org/10.1061/(asce)mt.1943-5533.0001666

Belda, A., Hornbostel, K., De Weerdt, K., & Rica, M. (2019). Macrocell corrosion in carbonated portland and portland-fly ash concrete—contribution and mechanism. *Cement and Concrete Research, 116*(2018), 273–283. https://doi.org/10.1016/j.cemconres.2018.12.005

Bertolini, L., Elsener, B., Pedeferri, P., Redaelli, E., & Polder, R. (2013). *Corrosion of Stell in Concrete: Prevention, Diagnosis and Repair* (W. VCH (ed.)

Bertolini, L., Pedeferri, P., Pastore, T., Bazzoni, B., & Lazzari, L. (1996). Macrocell effects on potential measurements in concrete cathodic protection systems. *Corrosion, 52*(7), 552–557. https://doi.org/10.5006/1.3292145

Blunt, J., Jen, G., & Ostertag, C. P. (2015). Enhancing corrosion resistance of reinforced concrete structures with hybrid fiber reinforced concrete. *Corrosion Science, 92*, 182–191. https://doi.org/10.1016/j.corsci.2014.12.003

Burkan-Isgor, O., Pour-Ghaz, M., & Ghods, P. (2009). The effect of temperature on the corrosion of steel in concrete. part 2: Model verification and parametric study. *Corrosion Science, 51*(2), 426–433. https://doi.org/10.1016/j.corsci.2008.10.036

Cadoni, E., Forni, D., Bonnet, E., & Dobrusky, S. (2019). Experimental study on direct tensile behaviour of UHPFRC under high strain-rates. *Construction and Building Materials, 218*, 667–680. https://doi.org/10.1016/j.conbuildmat.2019.05.152

Cao, C., & Cheung, M. M. S. (2014). Non-uniform rust expansion for chloride-induced pitting corrosion in RC structures. *Construction and Building Materials, 51*, 75–81. https://doi.org/10.1016/j.conbuildmat.2013.10.042

Cao, C., Cheung, M. M. S., & Chan, B. Y. B. (2013). Modelling of interaction between corrosion-induced concrete cover crack and steel corrosion rate. *Corrosion Science, 69*(24), 97–109. https://doi.org/10.1016/j.corsci.2012.11.028

Chalhoub, C., François, R., & Carcasses, M. (2020). Effect of cathode-anode distance and electrical resistivity on macrocell corrosion currents and cathodic response in cases of chloride induced corrosion in reinforced concrete structures. *Construction and Building Materials, 245*, 118337. https://doi.org/10.1016/j.conbuildmat.2020.118337

Chen, L., & Su, R. K. L. (2021). Corrosion rate measurement by using polarization resistance method for microcell and macrocell corrosion: theoretical analysis and experimental work with simulated concrete pore solution. *Construction and Building Materials, 267*, 121003. https://doi.org/10.1016/j.conbuildmat.2020.121003

Christodoulou, C., Goodier, C., Austin, S., Webb, J., & Glass, G. K. (2013). Diagnosing the cause of incipient anodes in repaired reinforced concrete structures. *Corrosion Science, 69*, 123–129. https://doi.org/10.1016/j.corsci.2012.11.032

Diao, B., Sun, Y., Ye, Y., & Cheng, S. (2012). Impact of seawater corrosion and freeze-thaw cycles on the behavior of eccentrically loaded reinforced

Lliso-Ferrando *et al. Int J Concr Struct Mater*   (2023) 17:15

Page 16 of 17

concrete columns. *Ocean Systems Engineering, 2*(2), 159–171. https://doi.org/10.12989/ose.2012.2.2.159

Dong, Z., & Poursaee, A. (2020). Corrosion behavior of coupled active and passive reinforcing steels in simulated concrete pore solution. *Construction and Building Materials, 240*, 117955. https://doi.org/10.1016/j.conbuildmat.2019.117955

Duffó, G. S., & Farina, S. B. (2016). Electrochemical behaviour of steel in mortar and in simulated pore solutions: analogies and differences. *Cement and Concrete Research, 88*, 211–216. https://doi.org/10.1016/j.cemconres.2016.07.007

Elsener, B. (2002). Macrocell corrosion of steel in concrete—implications for corrosion monitoring. *Cement and Concrete Composites, 24*(1), 65–72. https://doi.org/10.1016/S0958-9465(01)00027-0

European Union Funding for Research & Innovation. (2020). *Off-Shore Pilot Validation—Reshealience.* https://uhdc.eu/pilot-rdc-trl7/

Evans, U. R. (1978). The corrosion and oxidation of metals. *Edward Arnold.* https://doi.org/10.1002/maco.19780290130

Farzad, M., Garber, D., Azizinamini, A., & Lau, K. (2018). Corrosion macrocell development in reinforced concrete with repair UHPC. *NACE—International Corrosion Conference Series, 2018-April*(August)

Firouzi, A., & Rahai, A. (2013). Reliability assessment of concrete bridges subject to corrosion-induced cracks during life cycle using artificial neural networks. *Computers and Concrete, 12*(1), 91–107. https://doi.org/10.12989/cac.2013.12.1.091

François, R., Laurens, S., & Deby, F. (2018). *Corrosion and its consequences for reinforced concrete structures.* Amsterdam: ISTE Press Ltd. and Elsevier Ltd. https://doi.org/10.1016/c2016-0-01228-7

Gandía-Romero, J. M., Ramón, J. E., Bataller, R., Palací, D. G., Valcuende, M., & Soto, J. (2017). Influence of the area and distance between electrodes on resistivity measurements of concrete. *Materials and Structures/materiaux Et Constructions, 50*(1), 11527. https://doi.org/10.1617/s11527-016-0925-2

Gulikers, J. J. W. (1996). Experimental investigations on macrocell corrosion in chloride-contaminated concrete. *Heron, 41*(2), 107–123.

Habel, K., Viviani, M., Denarié, E., & Brühwiler, E. (2006). Development of the mechanical properties of an ultra-high performance fiber reinforced concrete (UHPFRC). *Cement and Concrete Research, 36*(7), 1362–1370. https://doi.org/10.1016/j.cemconres.2006.03.009

Hansson, C. M., Poursaee, A., & Laurent, A. (2006). Macrocell and microcell corrosion of steel in ordinary Portland cement and high performance concretes. *Cement and Concrete Composites, 36*(6), 2098–2102. https://doi.org/10.1016/j.cemconres.2006.07.005

Jaffer, S. J., & Hansson, C. M. (2008). The influence of cracks on chloride-induced corrosion of steel in ordinary Portland cement and high performance concretes subjected to different loading conditions. *Corrosion Science, 50*(12), 3343–3355. https://doi.org/10.1016/j.corsci.2008.09.018

Ji, Y., Hu, Y., Zhang, L., & Bao, Z. (2016). Laboratory studies on influence of transverse cracking on chloride-induced corrosion rate in concrete. *Cement and Concrete Composites, 69*, 28–37. https://doi.org/10.1016/j.cemconcomp.2015.12.006

Kang, S. T., & Kim, J. K. (2012). Investigation on the flexural behavior of UHPCC considering the effect of fiber orientation distribution. *Construction and Building Materials, 28*(1), 57–65. https://doi.org/10.1016/j.conbuildmat.2011.07.003

Kang, S. T., Lee, Y., Park, Y. D., & Kim, J. K. (2010). Tensile fracture properties of an ultra high performance fiber reinforced concrete (UHPFRC) with steel fiber. *Composite Structures, 92*(1), 61–71. https://doi.org/10.1016/j.compstruct.2009.06.012

Li, D., Wei, R., Li, L., Guan, X., & Mi, X. (2019). Pitting corrosion of reinforcing steel bars in chloride contaminated concrete. *Construction and Building Materials, 199*, 359–368. https://doi.org/10.1016/j.conbuildmat.2018.12.003

Lim, W. Y., & Hong, S. G. (2016). Shear tests for ultra-high performance fiber reinforced concrete (UHPFRC) beams with shear reinforcement. *International Journal of Concrete Structures and Materials, 10*(2), 177–188. https://doi.org/10.1007/s40069-016-0145-8

Liu, T., & Weyers, R. W. (1998). Modeling the dynamic corrosion process in chloride. *Cement and Concrete Research, 28*(3), 365–379.

Lliso-Ferrando, J. R., Martínez-Ibernón, A., Bataller, R., & Gandía-Romero, J. M. (2019). Passive layer destruction detection. Accumulated charge curve analysis. In: M. Adelaide Araújo, N. De Belie, & K. Van Tittelboom (Eds.), *Durable Concrete for Infrastructure under Severe Conditions: smart admixtures, self-responsiveness and nano-additions* (Issue September). Magnel Laboratory for Concrete Research

Lliso-Ferrando, J. R. (2022). *Monitorizacion de la durabilidad de estructuras existentes de hormigon armado mediante la inserción de una red de sensores.* Universitat Politècnica de València

Máca, P., Sovják, R., & Vavřiník, T. (2013). Experimental investigation of mechanical properties of UHPFRC. *Procedia Engineering, 65*, 14–19. https://doi.org/10.1016/j.proeng.2013.09.004

Mafalda, A., Chaves, S., Nunes, S., & Schlangen, E. (2021). Durability of an UHPFRC under mechanical and chloride loads. *Construction and Building Materials.* https://doi.org/10.1016/j.conbuildmat.2021.125223

Mansfeld, F. (1971). Area relationships in galvanic corrosion. *Corrosion, 27*(10), 436–442. https://doi.org/10.5006/0010-9312-27.10.436

Matos, A. M., Nunes, S., Chaves-Figueiredo, S., Schlangen, E., & Barroso-Aguilar, J. L. (2020). Chloride Ion Penetration into Cracked UHPFRC During Wetting-drying Cycles. In I. B. Valente, A. Ventura-Gouveia, & S. Dias (Eds.), *3rd RILEM Spring Convention and Conference (RSCC 2020)* (pp. 227–238). RILEM.

Michel, A., Solgaard, A. O. S., Pease, B. J., Geiker, M. R., Stang, H., & Olesen, J. F. (2013). Experimental investigation of the relation between damage at the concrete-steel interface and initiation of reinforcement corrosion in plain and fibre reinforced concrete. *Corrosion Science, 77*, 308–321. https://doi.org/10.1016/j.corsci.2013.08.019

Mir, Z. M., Höche, D., Gomes, C., Sampaio, R., Bastos, A. C., Maincon, P., Ferreira, M. G. S., & Zheludkevich, M. L. (2019). Enhanced predictive modelling of steel corrosion in concrete in submerged zone based on a dynamic activation approach. *International Journal of Concrete Structures and Materials.* https://doi.org/10.1186/s40069-018-0321-0

Mohammed, T. U., Otsuki, N., & Hamada, H. (2003). Corrosion of steel bars in cracked concrete under marine environment. *Journal of Materials in Civil Engineering, 15*(5), 460–469. https://doi.org/10.1061/(asce)0899-1561(2003)15:5(460)

Mohammed, T. U., Otsuki, N., Hisada, M., & Shibata, T. (2001). Effect of crack with and bar types on corrosion of steel in concrete. *Journal of Materials in Civil Engineering, 13*(3), 194–201.

Morga, M., & Marano, G. C. (2015). Chloride penetration in circular concrete columns. *International Journal of Concrete Structures and Materials, 9*(2), 173–183. https://doi.org/10.1007/s40069-014-0095-y

Nasser, A., Clément, A., Laurens, S., & Castel, A. (2010). Influence of steel-concrete interface condition on galvanic corrosion currents in carbonated concrete. *Corrosion Science, 52*(9), 2878–2890. https://doi.org/10.1016/j.corsci.2010.04.037

NORDTEST; Nordic Cooperation. (1999). NT Build 492. Rapid Chloride Migration Test (RCMT). *Nordtest Method*, 1–8

Paul, S. C., & van Zijl, G. P. A. G. (2017). Corrosion deterioration of steel in cracked SHCC. *International Journal of Concrete Structures and Materials, 11*(3), 557–572. https://doi.org/10.1007/s40069-017-0205-8

Pérez-Quiroz, J. T., Terán, J., Herrera, M. J., Martínez, M., & Genescá, J. (2008). Assessment of stainless steel reinforcement for concrete structures rehabilitation. *Journal of Constructional Steel Research, 64*(11), 1317–1324. https://doi.org/10.1016/j.jcsr.2008.07.024

Polder, R. B. (2009). Critical chloride content for reinforced concrete and its relationship to concrete resistivity. *Materials and Corrosion, 60*(8), 623–630. https://doi.org/10.1002/maco.200905302

Pour-Ghaz, M., Isgor, O. B., & Ghods, P. (2009). The effect of temperature on the corrosion of steel in concrete part 1: simulated polarization resistance tests and model development. *Corrosion Science, 51*(2), 415–425. https://doi.org/10.1016/j.corsci.2008.10.034

Poursaee, A., & Hansson, C. M. (2009). Potential pitfalls in assessing chloride-induced corrosion of steel in concrete. *Cement and Concrete Research, 39*(5), 391–400. https://doi.org/10.1016/j.cemconres.2009.01.015

Qian, S., Zhang, J., & Qu, D. (2006). Theoretical and experimental study of microcell and macrocell corrosion in patch repairs of concrete structures. *Cement and Concrete Composites, 28*, 685–695. https://doi.org/10.1016/j.cemconcomp.2006.05.010

Raupach, M. (1996). Chloride-induced macrocell corrosion of steel in concrete–theoretical background and practical consequences. *Construction and Building Materials, 10*(5), 329–338.

Ribeiro, J. L. S., Panossian, Z., & Selmo, S. M. S. (2013). Proposed criterion to assess the electrochemical behavior of carbon steel reinforcements under corrosion in carbonated concrete structures after patch repairs.

Construction and Building Materials, 40, 40–49. https://doi.org/10.1016/j.conbuildmat.2012.09.097

Sangoju, B., Gettu, R., Bharatkumar, B. H., & Neelamegam, M. (2011). Chloride-induced corrosion of steel in cracked OPC and PPC concretes: experimental study. *Journal of Materials in Civil Engineering, 23*(7), 1057–1066. https://doi.org/10.1061/(asce)mt.1943-5533.0000260

Scheydt, J. C., & Muller, H. S. (2012). Microstructure of ultra high performance concrete (UHPC) and its impact on durability. In: M. Schmidt, E. Fehling, C. Glotzbach, S. Fröhlich, S. Piotrowski(Eds.), *Proceedings of the 3rd International Symposium on UHPC and Nanotechnology for High Performance Construction Materials*, 349–356

Serna, P., Lo Monte, F., Mezquida-Alcaraz, E. J., Cuenca, E., Mechtcherine, V., & Reichardt, M. (2019). Upgrading the concept of UHPFRC for high durability in the cracked state: the concept of ultra high durability cincrete (UHDC) in the approach of the H2020 project reshealience. *RILEM Publications SARL, 128*(Sustainable materials systems and structures), 764–771.

Shafieifar, M., Farzad, M., & Azizinamini, A. (2017). Experimental and numerical study on mechanical properties of ultra high performance concrete (UHPC). *Construction and Building Materials, 156*, 402–411. https://doi.org/10.1016/j.conbuildmat.2017.08.170

Shaikh, F. U. A. (2018). Effect of cracking on corrosion of steel in concrete. *International Journal of Concrete Structures and Materials*. https://doi.org/10.1186/s40069-018-0234-y

Shin, H. O., Lee, S. J., & Yoo, D. Y. (2018). Bond behavior of pretensioned strand embedded in ultra-high-performance fiber-reinforced concrete. *International Journal of Concrete Structures and Materials*. https://doi.org/10.1186/s40069-018-0249-4

Soleimani, S., Ghods, P., Isgor, O. B., & Zhang, J. (2010). Modeling the kinetics of corrosion in concrete patch repairs and identification of governing parameters. *Cement and Concrete Composites, 32*(5), 360–368. https://doi.org/10.1016/j.cemconcomp.2010.02.001

Stern, M. (1957). Closure to "Discussion of 'Electrochemical Polarization, 1. A Theoretical Analysis of the Shape of Polarization Curves' M. Stern and A. L. Geary." *Journal of The Electrochemical Society*, *104*(12), 751. https://doi.org/10.1149/1.2428473

Subramaniam, K. V., & Bi, M. (2010). Investigation of steel corrosion in cracked concrete: evaluation of macrocell and microcell rates using tafel polarization response. *Corrosion Science, 52*(8), 2725–2735. https://doi.org/10.1016/j.corsci.2010.04.030

Suesta, C., Lisardo, F., Scalari, S., Animato, F., Camacho, E., Deegan, P., Borg, R. P., Ferrara, L., & Alonso, M. C. (2018). *Reshealience: Rethinking coastal defence and Green-energy Service infrastructures through enHancEd-durAbiLity high-performance cement-based materials. Report.* https://uhdc.eu/resources/

Trejo, D., & Monteiro, P. J. (2005). Corrosion performance of conventional (ASTM A615) and low-alloy (ASTM A706) reinforcing bars embedded in concrete and exposed to chloride environments. *Cement and Concrete Research, 35*(3), 562–571. https://doi.org/10.1016/j.cemconres.2004.06.004

Valcuende, M., Lliso-Ferrando, J. R., Ramón-Zamora, J. E., & Soto, J. (2021a). Corrosion resistance of ultra-high performance fibre—reinforced concrete. *Construction and Building Materials*. https://doi.org/10.1016/j.conbuildmat.2021a.124914

Valcuende, M., Lliso-Ferrando, J. R., Roig-Flores, M., & Gandía-Romero, J. M. (2021b). Porous structure of ultra-high-performance fibre-reinforced concretes. *Materials, 14*, 1637. https://doi.org/10.3390/ma14071637

Warkus, J., & Raupach, M. (2006). Modelling of reinforcement corrosion—corrosion with extensive cathodes. *Materials and Corrosion, 57*(12), 920–925. https://doi.org/10.1002/maco.200604032

Warkus, J., Brem, M. & Raupach, M. (2006). BEM-models for the propagation period of chloride inducedreinforcement corrosion. *Materials and Corrosion, 57*, 636–641. https://doi.org/10.1002/maco.200603995

Warkus, J., & Raupach, M. (2010). Modelling of reinforcement corrosion—geometrical effects on macrocell corrosion. *Materials and Corrosion, 61*(6), 494–504. https://doi.org/10.1002/maco.200905437

Wu, X., Kang, T. H. K., Mpalla, I. B., & Kim, C. S. (2018). Axial load testing of hybrid concrete columns consisting of UHPFRC tube and normal-strength concrete core. *International Journal of Concrete Structures and Materials*. https://doi.org/10.1186/s40069-018-0275-2

Yoo, D. Y., & Yoon, Y. S. (2016). A review on structural behavior, design, and application of ultra-high-performance fiber-reinforced concrete. *International Journal of Concrete Structures and Materials, 10*(2), 125–142. https://doi.org/10.1007/s40069-016-0143-x

Zhang, H., Ji, T., Zeng, X., Yang, Z., Lin, X., & Liang, Y. (2018). Mechanical behavior of ultra-high performance concrete (UHPC) using recycled fine aggregate cured under different conditions and the mechanism based on integrated microstructural parameters. *Construction and Building Materials, 192*, 489–507. https://doi.org/10.1016/j.conbuildmat.2018.10.117

Zhou, Y., Gencturk, B., Willam, K., & Attar, A. (2015). Carbonation-induced and chloride-induced corrosion in reinforced concrete structures. *Journal of Materials in Civil Engineering, 27*(9), 04014245. https://doi.org/10.1061/(asce)mt.1943-5533.0001209

Publisher's Note

Springer Nature remains neutral with regard to jurisdictional claims in published maps and institutional affiliations.